Study of the Annealing Effect on the γ-Phase Aluminum Oxide Films Prepared by the High-Vacuum MOCVD System

Zhao Li [ID], Yangmei Xin, Yunyan Liu, Huiqiang Liu [ID], Dan Yu * and Junshan Xiu *

School of Physics and Optoelectronic Engineering, Shandong University of Technology, Zibo 255000, China; zli@sdut.edu.cn (Z.L.); xinyangmei8@163.com (Y.X.); liuyysdut@163.com (Y.L.); liuhq@sdut.edu.cn (H.L.)
* Correspondence: yudan@sdut.edu.cn (D.Y.); xiujunshan@126.com (J.X.)

Abstract: γ-phase aluminum oxide (γ-Al_2O_3) films are grown on MgO (100) wafers by metal organic chemical vapor deposition (MOCVD). Post-annealing process is conducted to study the influence of annealing temperature on the properties of the films. Structural analyses indicate that all the deposited and annealed films present a preferred growth orientation of γ-Al_2O_3 (220) along the MgO (200) direction. And the film annealed at 1100 °C exhibits the best film quality compared with those of the films grown and annealed at other temperatures. Scanning electron microscopy measurements also imply the best surface morphology for the γ-Al_2O_3 film annealed at 1100 °C, which is in good accordance with the structural analyses. Optical transmittance spectra show good transparency for all the deposited and annealed films in the visible wavelength region with an average transmittance value of 83.5%. The optical bandgaps are estimated to be in the range of 5.56–5.79 eV for the deposited and annealed films. Semiconductor films with high optical transmittance in the visible region as well as wide bandgaps are appropriate for the manufacture of transparent optoelectronic devices and ultraviolet optoelectronic devices.

Keywords: MOCVD; thin films; annealing; MgO substrates; structural properties

1. Introduction

Oxide semiconductor materials with wide bandgap have a wide range of applications in short-wavelength light-emitting devices, ultraviolet detectors, solar cells, and thin film transistors [1–4], which have aroused people's research interest in recent years. Compared with traditional wide band gap oxide materials, such as ITO [5] and ZnO [6], aluminum oxide (Al_2O_3) has a wider band gap (~8.7 eV) and relatively stable physical and chemical properties [7]. In addition, Al_2O_3 also has the advantages of high relative hardness (Mohs scale, ~8.8), high breakdown field strength (6–8 MV/cm), high dielectric constant (~9), easy preparation, and low cost, which can be very suitable for manufacturing ultraviolet optoelectronic devices and transparent optoelectronic devices [8,9].

There are many polymorphs of Al_2O_3, such as α-phase (hexagonal) [10], γ-phase (cubic) [11], δ-phase (tetragonal or orthogonal) [12], θ-phase (monoclinic) [13] and κ-phase (orthogonal) [14], two of which are the most common crystal forms, γ-Al_2O_3 and α-Al_2O_3. The various phases can be converted to each other due to the differences in temperature and preparation methods [15], but almost all other phases are converted into α-Al_2O_3 at high temperatures above 1300 °C. Al_2O_3 is widely used in many fields. It can be used as abrasive materials and cutting tools and can also be applied to make high-temperature refractory materials and antireflection coatings on glass surfaces [16,17]. α-phase Al_2O_3 is usually applied as substrates for growing film materials [18,19]. γ-Al_2O_3 is also widely used, mainly as coatings, adsorbents, and soft abrasives [20,21]. It plays a more important role in the chemical industry and is often used as a catalyst support material for energy generation and storage [22]. In recent years, the preparations of Al_2O_3 thin films and their doped materials and the studies of their luminescence properties have attracted widespread interest. Al_2O_3 can emit fluorescence of different wavelengths through the

doping of transition metal elements and rare earth elements [23,24] and has possible application prospects in the fields of optical communications, lasers, integrated optics, and panel displays [25,26].

The common preparation methods of Al_2O_3 film are including magnetron sputtering [27], plasma deposition [28], sol-gel [29], spray pyrolysis [30], electron beam evaporation [31], pulsed laser deposition [32] and metal organic chemical vapor deposition (MOCVD) [33]. MOCVD is a method of vapor phase epitaxial growth using organic metal thermal decomposition reaction. It has simple reaction equipment, wide growth temperature range, precise control of deposition parameters, and raw material gas which will not affect the film. Advantages such as obvious changes in doping concentration can be achieved along the film growth. Oxide films prepared by MOCVD are widely used in the electronics industry. Therefore, MOCVD method is applied in this work to grow Al_2O_3 films. The preparation temperature of the crystalline Al_2O_3 films is generally very high. It is reported in the literature that post-annealing is a very effective way to improve the performance of the film [34]. The structure and optical properties of the films can be greatly improved after annealing [35]. In view of the fact that the maximum deposition temperature of the MOCVD equipment applied in our experiment is below 750 °C, the substrate temperature for preparing the alumina films in the experiment is set to be 700 °C. And then the prepared samples are annealed subsequently. The impact of annealing temperature on the structural and optical properties of the Al_2O_3 films was studied systematically in this paper.

2. Experimental Details

The series of Al_2O_3 films were deposited using a homemade MOCVD system. The oxidant used in the work is O_2 [purity: 99.999% (5N)]. The carrier gas is high-purity N_2 (5N), which will be purified to 9N by an inert gas purifier before entering the system. The metalorganic (MO) source used in this experiment is trimethylaluminum (TMAl) [$Al(CH_3)_3$] with a purity of 6N, which is placed in a stainless steel source bottle in a cold trap. The gas transportation pipeline is made of high-quality stainless steel pipes polished inside and outside, connected by Swagelok VCR joints and special metal gaskets to ensure the airtightness of the gas pipeline. The flow of each pipeline gas is accurately controlled by a mass flow controller and an electrical pressure controller. The reaction chamber adopts a dual-air flow mode. The N_2 carries MO steam from the side wall and flows into the top of the substrate, and the other N_2 carries O_2 into the reaction chamber through a nozzle from directly above the reaction chamber. This dual-air flow mode can not only suppress the thermal convection effect, but also press the reactants to the substrate, improving the deposition rate and film uniformity. The molar flow rate of MO steam is determined jointly by the vapor pressure of the organic source at a specific temperature, the pressure of the MO source bottle, and the flow of the carrier gas carrying the MO vapor. The MgO substrates were cut to the required size (10 mm × 10 mm) by a diamond cutter, then cleaned with an ultrasonic bath of acetone, alcohol, and deionized water, followed by blow-drying with nitrogen flow for use. Upon the growth process (5 h), the deposition temperature and chamber pressure were kept at 700 °C and 35 mbar, respectively. The molar flow rates of the TMAl and O_2 were calculated as 2.3×10^{-6} and 2.23×10^{-3} mol/min. After the growth process, the films were taken out of the chamber and post-annealed under air in a tube furnace for 1 h at temperatures of 900, 1000, 1100 °C.

The crystal structure of the films was studied using X-ray diffraction measurement by a Rigaku D/max-rB diffractometer (Rigaku, Tokyo, JPN) with an X-ray wavelength of 1.5406 Å in the 2θ range of 10°–80°. The SEM measurements of the films were taken using FEI Nova Nano SEM-450 (Hillsboro, OR, USA) to study the surface morphology. The thickness of the samples was observed by cross-sectional SEM measurement. Chemical analysis was carried out by X-ray photoelectron spectroscopy (XPS) using a Thermo Scientific ESCALAB 250 XI spectrometer (Waltham, MA, USA). Ultraviolet-visible (UV-VIS) transmission spectroscopy was conducted by using a TU-1901 double-beam UV-VIS

spectrophotometer (General Analytical, Beijing, China) to analyze the optical properties of the films.

3. Results and Discussion

The chemical compositions of the Al_2O_3 films are investigated by XPS measurements. Figure 1a indicates the XPS survey-scan spectrum of the as-deposited Al_2O_3 film, where the binding energy peaks of C 1s, Al 2s, Al 2p, O 1s, O KLL can be observed. The energy peak of C 1s may be attributed to the adventitious hydrocarbon contamination or the carbon dioxide adsorption on the surface of the film. No signal of energy peaks of elements other than Al, O, C is detected, indicating that the prepared films are aluminum oxide films. The calibration of the peak position is commonly used by the reference of C 1s core level at a binding energy of 284.6 eV [36]. Spectra (b) and (c) are the high-resolution energy peaks of Al 2p and O 1s core levels. As can be seen in Figure 1b, the aluminum core level of Al 2p is located at 74.6 eV, being in accordance with the references related to Al_2O_3 [29,37]. Furthermore, the Al 2p peak presents a symmetrical spectrum without any obvious Al–Al peak, indicating the absence of dissociative Al ions in our as-deposited film. The O 1s core level shown in Figure 1c can be divided into two peaks by Gaussian fitting. The peak located at a low binding energy of 530.7 eV can be designated as Al–O bonding in Al_2O_3 lattice. While the other peak located at a high binding energy of 532.3 eV may be attributed to the presence of loosely bound oxygen of adsorbed carbonyl and/or carbon-oxygen compounds on the film surface [38]. Quantitative analyses are studied based on estimated areas of O 1s (fit peak of the low binding energy of 530.7 eV) and Al 2p core levels by the elemental sensitivity factor method. The atomic ratio of O and Al is determined as 1.56, which is consistent with the stoichiometry of pure Al_2O_3.
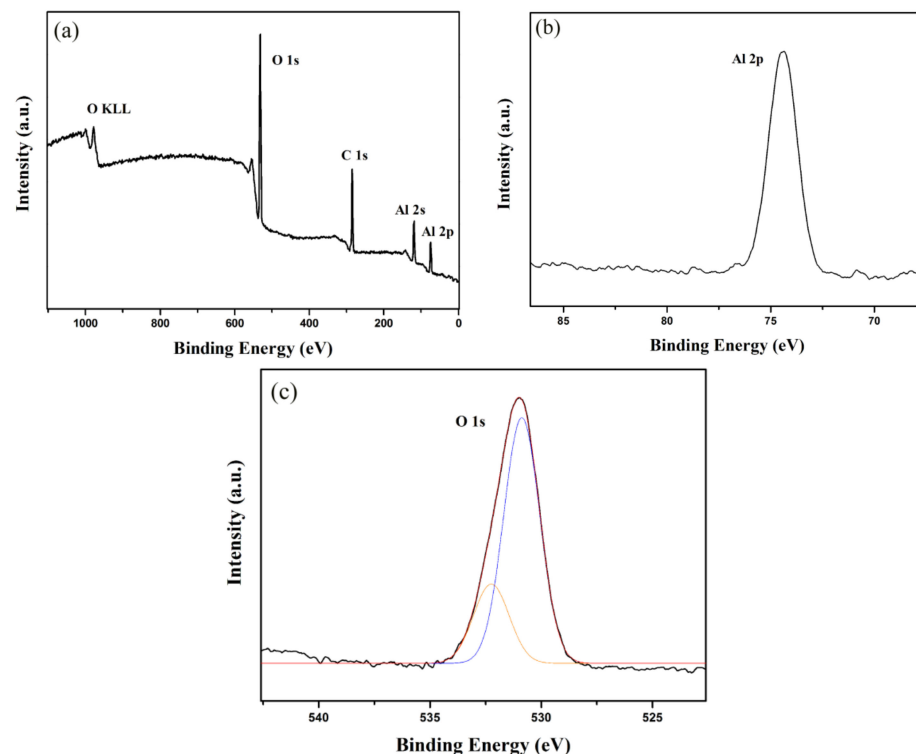
Figure 1. X-ray photoelectron spectroscopy (XPS) spectra of the as-deposited Al_2O_3 film: (**a**) survey spectrum, high-resolution spectra of (**b**) Al 2p and (**c**) O 1s.

Figure 2 shows the XRD patterns of (Figure 2a) the as-grown aluminum oxide film and the post-annealed ones at different annealing temperatures of (Figure 2b) 900 °C, (Figure 2c) 1000 °C, and (Figure 2d) 1100 °C in air, respectively.
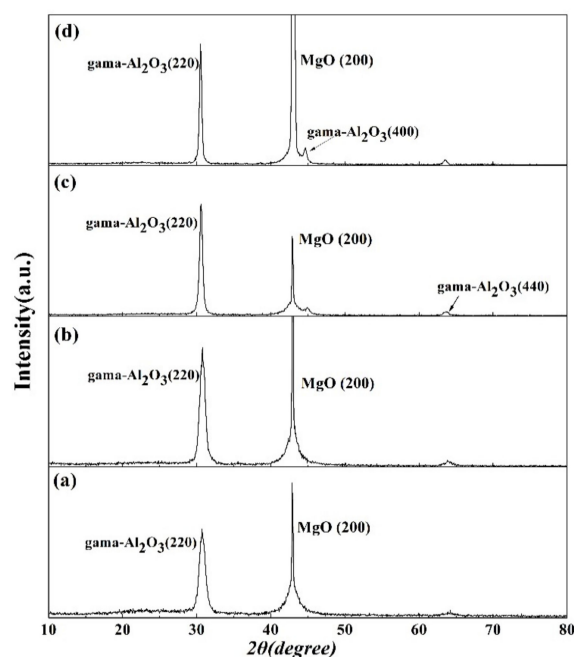
Figure 2. XRD spectra of Al_2O_3 films of (**a**) the as-grown and post-annealed at temperatures of (**b**) 900 °C, (**c**) 1000 °C and (**d**) 1100 °C.

It can be seen from the patterns of all the deposited and annealed films, besides the diffraction peaks of the MgO (200) substrates, only signals corresponding to cubic γ-phase Al_2O_3 (JCPDS #50-0741) are detected with diffractions of (220), (200) and (440) planes. The intensity of the (200) and (440) peaks is rather weak compared with that of the (220) peak, and the (220) peak is the predominant reflection, as is revealed in the spectra. All the films present a preferential growth orientation of γ-Al_2O_3 (220) along the MgO (200) direction. Note that a slight shift towards lower angle direction of the (220) peak can be observed in Figure 2, implying a systematic lattice expansion, which is also reported previously [39,40]. As we all know, commonly, material has a certain flexibility. The lattice expansion may be attributed to the release of pressure stress in the inner part of the films after heat treatment. As for the annealed films, the intensity of the (220) peaks is more intense, and the full width at half maximum (FWHM) of (220) peaks are measured to be 0.915°, 0.537°, and 0.373°, corresponding to annealing temperatures of 900, 1000, and 1100 °C, respectively, which is rather smaller than that of as deposited film with a value of 1.038°. The FWHM is a reflection of the film crystallinity. Lower FWHM corresponds to higher film crystallinity. The decrease of the FWHM with the increasing annealing temperature reveals the improvement of the film crystallinity, which can be attributed to the recrystallization process in the films at high temperatures [41]. The average particle size (*D*) of the Al_2O_3 films is determined by Scherrer equation [42],

$$D = k\lambda/b\cos\theta \qquad (1)$$

where *k* is a crystalline shape-related constant and usually taken as 0.9, λ is the X-ray wavelength applied in the diffractometer (0.15406 nm), *b* is the FWHM of γ-Al_2O_3 (220) plane in radian, and θ is Bragg's angle of the corresponding (220) peak. The variations of *b* and *D* values calculated using Al_2O_3 (220) plane as a function of annealing temperature are illustrated in Figure 3. As can be seen, the average grain size of the film presents a monotonous increase with the increasing annealing temperature, reaching a maximum value of 22.5 nm for the film annealed at 1100 °C. It is believed that the increase of the average particle size may be attributed to the coalescence of small grains caused by the increasing kinetic energy with the increasing annealing temperature. All the results reveal that the annealing process

exhibits a prominent influence on the crystal structure of the film, and the sample annealed at the temperature of 1100 °C exhibits the best crystalline quality.
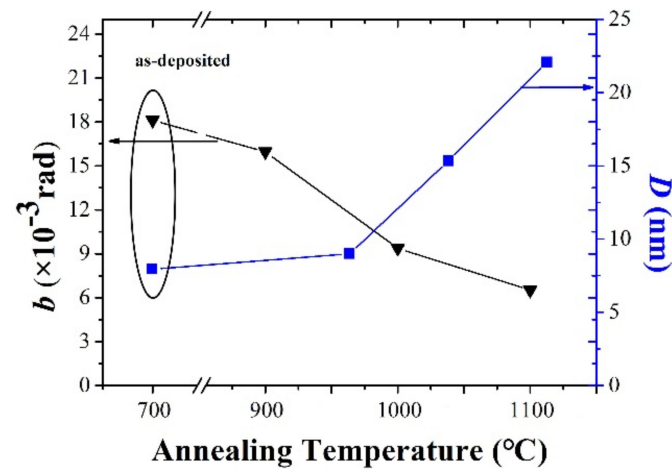
Figure 3. The full width at half maximum (*b*) and average grain size (*D*) values as a function of annealing temperature.

The surface morphologies of Al_2O_3 films are studied by SEM with top-view images. Images (a)–(d) of Figure 4 are corresponding to the as-deposited Al_2O_3 film and the ones post-annealed at 900, 1000, and 1100 °C, respectively. The inset shows the cross-sectional SEM image of the as-deposited Al_2O_3 film, where the thickness of the deposited film can be obtained to be about 180 nm. As shown in Figure 4a, a leaf-shaped structure is presented for the as-deposited Al_2O_3 film, exhibiting the coalescence of some small grains. For the annealed films at 900 and 1000 °C, illustrated in Figure 4b,c, the compact textures comprised of both large and small grains are revealed on the MgO substrates. The SEM image of the film annealed at 1100 °C, which is shown in Figure 4d, indicates the homogeneous and oriented grain growth with a clear and regular edge through the film. Closely packed polygonal-shaped grains with larger size have developed on top of the substrate. As clearly observed in the images, the average particle size increases with the increasing annealing temperature, which is consistent with the XRD analyses. The annealing temperature exhibits a remarkable influence on the surface morphology of Al_2O_3 films.
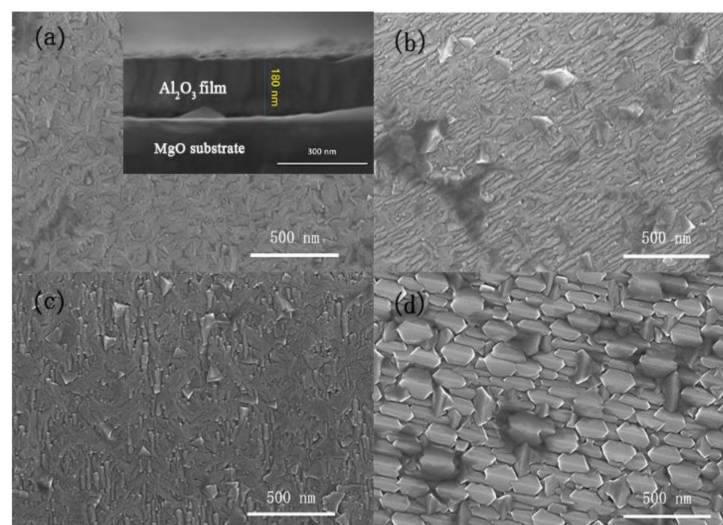
Figure 4. Top-view SEM images of (**a**) the as-deposited Al_2O_3 film, and post-annealed ones at temperatures of (**b**) 900 °C, (**c**) 1000 °C and (**d**) 1100 °C, with the cross-sectional SEM image of the as-deposited Al_2O_3 film in the inset.

Figure 5a shows the transmittance spectra of the as-grown and post-annealed Al_2O_3 films at different temperatures. The mean values of optical transmittance for all the films in the visible wavelength region (380–800 nm) are calculated above 83.5%, which reveals their good optical transparency. The good transmittance exhibited supports the suitability of their applications as flat panel display devices. The oscillations observed in the transmittance spectra are the sign of the interference between two interfaces of air film and film substrate. The absorption edge of the film shifts toward the long wavelength direction with the increasing annealing temperature, indicating the narrowing of the optical bandgap (E_g). The absorption coefficient (α) is related with optical transmittance (T) by the equation [43],

$$\alpha = \left\{ \ln[(1-R)^2/T] \right\}/d \tag{2}$$

where d is the thickness, R stands for the reflectance, which can be neglected ($R << 1$). The E_g dependence of the α is given by the Tauc equation [44],

$$(\alpha h\nu)^2 = A(h\nu - E_g) \tag{3}$$

where $h\nu$ indicates the incident photo energy, and A is a constant related to the band edge. Figure 5b shows the plot of $(\alpha h\nu)^2$ versus $h\nu$, where the E_g can be estimated at the crossing point between the line extrapolated from the linear part of the curve and $h\nu$-axis of the plot. The optical bandgaps are found to be 5.79, 5.73, 5.65, and 5.56 eV, corresponding to the as-grown and 900, 1000, and 1100 °C annealed samples, respectively. First-principles calculations indicate that the actual optical band gap of γ-phase Al_2O_3 film is much lower than the theoretical value [45,46]. Some researchers have reported the optical bandgap values of Al_2O_3 films as 5.36 eV [47], 5.50–5.63 eV [48,49], and 5.80–5.89 eV [30], which is in good accordance with the results obtained in this work. As can be seen, the E_g of the film decreases with the increase of the annealing temperature, which is consistent with the improvement of the structural properties of the film revealed in the XRD results. The explanation may be attributed to the sufficient energy supplied by thermal annealing which can cure the randomness of inner atoms into the films, increasing the degree of atomic ordering [50].
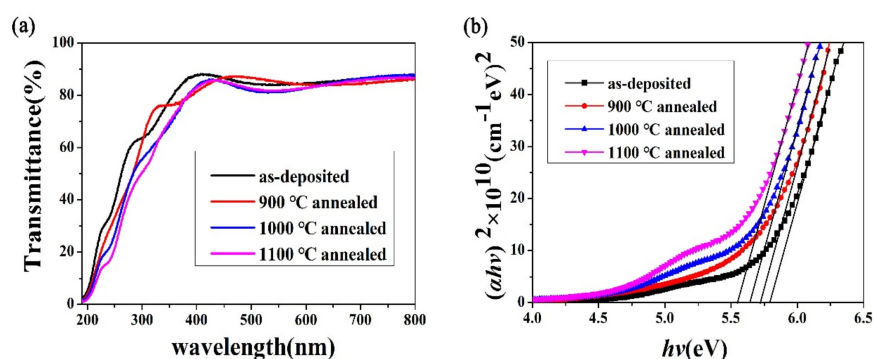

Figure 5. (**a**) Optical transmittance spectra of the as-grown Al_2O_3 film and the post-annealed ones at temperatures of 900, 1000 and 1100 °C, (**b**) $(\alpha h\nu)^2$ vs. $h\nu$ of the corresponding samples.

4. Conclusions

In general, MOCVD technique has been applied to grow γ-Al_2O_3 films on MgO (100) substrates, followed by post-annealing at temperatures of 900, 1000, and 1100 °C. XPS study confirmed the stoichiometry of pure Al_2O_3 without dissociative Al ions. The annealing temperature had a great impact on the structural and optical properties of the films. The best crystallization and surface morphology were observed at the annealing temperature of 1100 °C, with the maximum value of the average particle size of the films. All the films presented a preferred growth orientation of γ-Al_2O_3 (220)//MgO (200). The average transmittance of the as-grown and post-annealed γ-Al_2O_3 films in the visible

region exceeded 83.5%. The optical bandgaps of the films are found to be ranging from 5.56 to 5.79 eV. Al_2O_3 film materials with fine performances can be used in many fields such as transparent photoelectrical devices, solar cells, flat panel displays, and UV light detectors.

Author Contributions: Conceptualization, Z.L. and J.X.; methodology, Z.L.; software, Y.L.; formal analysis, J.X.; investigation, Y.X.; data curation, Y.X.; writing—original draft preparation, Z.L.; writing—review and editing, J.X.; project administration, D.Y.; funding acquisition, H.L. All authors have read and agreed to the published version of the manuscript.

Conflicts of Interest: There are no known competing financial interests or personal relationships that could have appeared to influence the work reported in this paper.

References

1. Sun, Y.R.; Giebink, N.C.; Kanno, H.; Ma, B.W.; Thompson, M.E.; Forrest, S.R. Management of singlet and triplet excitons for efficient white organic light-emitting devices. *Nat. Cell Biol.* **2006**, *440*, 908–912. [CrossRef]
2. Peng, W.; He, Y.; Wen, C.; Ma, K. Surface acoustic wave ultraviolet detector based on zinc oxide nanowire sensing layer. *Sens. Actuators A Phys.* **2012**, *184*, 34–40. [CrossRef]
3. Jeong, S.; Jeong, Y.; Moon, J. Solution-processed zinc tin oxide semiconductor for thin-film transistors. *J. Phys. Chem. C* **2008**, *112*, 11082–11085. [CrossRef]
4. Hara, K.; Horiguchi, T.; Kinoshita, T.; Sayama, K.; Sugihara, H.; Arakawa, H. Highly efficient photon-to-electron conversion with mercurochrome-sensitized nanoporous oxide semiconductor solar cells. *Sol. Energy Mater. Sol. Cells* **2000**, *64*, 115–134. [CrossRef]
5. Kim, K.; Park, J.H.; Kim, H.; Kim, J.K.; Schubert, E.F.; Cho, J. Energy bandgap variation in oblique angle-deposited indium tin oxide. *Appl. Phys. Lett.* **2016**, *108*, 041910. [CrossRef]
6. Ansari, S.A.; Khan, M.M.; Kalathil, S.; Nisar, A.; Lee, J.; Cho, M.H. Oxygen vacancy induced band gap narrowing of ZnO nanostructures by an electrochemically active biofilm. *Nanoscale* **2013**, *5*, 9238–9246. [CrossRef] [PubMed]
7. Othman, H.; Valiev, D.; Polisadova, E. Structural and mechanical properties of zinc aluminoborate glasses with different content of aluminum oxide. *J. Mater. Sci. Mater. Electron.* **2017**, *28*, 4647–4653. [CrossRef]
8. Lee, B.R.; Lee, T.H.; Son, K.-R.; Kim, T.G. ITO/Ag/AlN/Al_2O_3 multilayer electrodes with conductive channels: Application in ultraviolet light-emitting diodes. *J. Alloys Compd.* **2018**, *741*, 21–27. [CrossRef]
9. Zhang, G.Z.; Wu, H.; Chen, C.; Wang, T.; Wang, P.Y.; Mai, L.Q.; Yue, J.; Liu, C. Transparent capacitors based on nanolaminate Al_2O_3/TiO_2/Al_2O_3 with H_2O and O_3 as oxidizers. *Appl. Phys. Lett.* **2014**, *104*, 163503. [CrossRef]
10. Eng, P.J.; Trainor, T.P.; Brown, G.E., Jr.; Waychunas, G.A.; Newville, M.; Sutton, S.R.; Rivers, M.L. Structure of the hydrated α-Al_2O_3 (0001) surface. *Science* **2000**, *288*, 1029–1033. [CrossRef]
11. Chou, T.C.; Nieh, T.G. Nucleation and concurrent anomalous grain growth of α-Al_2O_3 during γ-α phase transformation. *J. Am. Ceram. Soc.* **1991**, *74*, 2270–2279. [CrossRef]
12. Paunović, N.; Dohčević-Mitrović, Z.; Scurtu, R.; Aškrabić, S.; Prekajski, M.; Matović, B.; Popović, Z.V. Suppression of inherent ferromagnetism in Pr-doped CeO_2 nanocrystals. *Nanoscale* **2012**, *4*, 5469–5476. [CrossRef]
13. Jbara, A.S.; Othaman, Z.; Saeed, M. Structural, morphological and optical investigations of θ-Al_2O_3 ultrafine powder. *J. Alloys Compd.* **2017**, *718*, 1–6. [CrossRef]
14. Belonoshko, A.B.; Ahuja, R.; Johansson, B. Mechanism for the $\kappa-Al_2O_3$ to the $\alpha-Al_2O_3$ transition and the stability of κ-Al_2O_3 under volume expansion. *Phys. Rev. B* **2000**, *61*, 3131. [CrossRef]
15. Santos, P.S.; Santos, H.S.; Toledo, S.P. Standard transition aluminas. Electron microscopy studies. *Mater. Res.* **2000**, *3*, 104–114. [CrossRef]
16. Musante, L.; Munoz, V.; Labadie, M.H.; Tomba-Martinez, A.G. High temperature mechanical behavior of Al_2O_3–MgO–C refractories for steelmaking use. *Ceram. Int.* **2011**, *37*, 1473–1483. [CrossRef]
17. Kauppinen, C.; Isakov, K.; Sopanen, M. Grass-like alumina with low refractive index for scalable, broadband, omnidirectional antireflection coatings on glass using atomic layer deposition. *ACS Appl. Mater. Interfaces* **2017**, *9*, 15038–15043. [CrossRef] [PubMed]
18. Wojewoda-Budka, J.; Sobczak, N.; Morgiel, J.; Nowak, R. Microstructure characteristics of the reaction product region formed due to the high temperature contact of molten aluminium and ZnO single crystal. *Solid State Phenom.* **2011**, *172–174*, 1267–1272. [CrossRef]
19. Shen, P.; Fujii, H.; Matsumoto, T.; Nogi, K. Surface orientation and wetting phenomena in Si/α-alumina system at 1723 K. *J. Am. Ceram. Soc.* **2005**, *88*, 912–917. [CrossRef]
20. Jiang, Z.; Yang, X.; Liang, Y.; Hao, G.; Zhang, H.; Lin, J. Favorable deposition of γ-Al_2O_3 coatings by cathode plasma electrolysis for high-temperature application of Ti-45Al-8.5Nb alloys. *Surf. Coat. Technol.* **2018**, *333*, 187–194. [CrossRef]
21. Tabesh, S.; Davar, F.; Loghman-Estarki, M.R. Preparation of γ-Al_2O_3 nanoparticles using modified sol-gel method and its use for the adsorption of lead and cadmium ions. *J. Alloys Compd.* **2018**, *730*, 441–449. [CrossRef]

22. Lelo, R.V.; Maron, G.K.; Thesing, A.; Alano, J.H.; Rodrigues, L.D.S.; Noremberg, B.D.S.; Escote, M.T.; Valentini, A.; Probst, L.F.D.; Carreño, N.L.V. Vanadium effect over γ-Al$_2$O$_3$-supported Ni catalysts for valorization of glycerol. *Fuel Process. Technol.* **2021**, *216*, 106773. [CrossRef]

23. He, Y.; He, J.; Zhang, H.; Liu, Y.; Lei, B. Luminescent properties and energy transfer of luminescent carbon dots assembled mesoporous Al$_2$O$_3$: Eu^{3+} co-doped materials for temperature sensing. *J. Colloid Interface Sci.* **2017**, *496*, 8–15. [CrossRef]

24. Wang, X.; Hu, L.; Meng, X.; Li, H.; Wang, S. Effect of Al$_2$O$_3$ and La$_2$O$_3$ on structure and spectroscopic properties of Nd-doped sol–gel silica glasses. *J. Lumin.* **2018**, *204*, 554–559. [CrossRef]

25. Lakshminarayana, G.; Ruan, J.; Qiu, J. NIR luminescence from Er–Yb, Bi–Yb and Bi–Nd codoped germanate glasses for optical amplification. *J. Alloys Compd.* **2009**, *476*, 878–883. [CrossRef]

26. He, L.; Pan, L.; Li, W.; Dong, Q.; Sun, W. Spectral response characteristics of Eu^{3+} doped YAG-Al$_2$O$_3$ composite nanofibers reinforced aluminum matrix composites. *Opt. Mater.* **2020**, *104*, 109845. [CrossRef]

27. Ding, J.C.; Zhang, T.F.; Mane, R.S.; Kim, K.-H.; Kang, M.C.; Zou, C.W.; Wang, Q.M. Low-temperature deposition of nanocrystalline Al$_2$O$_3$ films by ion source-assisted magnetron sputtering. *Vacuum* **2018**, *149*, 284–290. [CrossRef]

28. Haiying, W.E.; Hongge, G.U.; Lijun, S.A.; Xingcun, L.I.; Qiang, C.H. Study on deposition of Al$_2$O$_3$ films by plasma-assisted atomic layer with different plasma sources. *Plasma Sci. Technol.* **2018**, *20*, 065508.

29. Hu, B.; Yao, M.; Xiao, R.; Chen, J.; Yao, X. Optical properties of amorphous Al$_2$O$_3$ thin films prepared by a sol–gel process. *Ceram. Int.* **2014**, *40*, 14133–14139. [CrossRef]

30. Dhonge, B.P.; Mathews, T.; Sundari, S.T.; Thinaharan, C.; Kamruddin, M.; Dash, S.; Tyagi, A. Spray pyrolytic deposition of transparent aluminum oxide (Al$_2$O$_3$) films. *Appl. Surf. Sci.* **2011**, *258*, 1091–1096. [CrossRef]

31. Shuzhen, S.; Lei, C.; Haihong, H.; Kui, Y.; Zhengxiu, F.; Jianda, S. Annealing effects on electron-beam evaporated Al$_2$O$_3$ films. *Appl. Surf. Sci.* **2005**, *242*, 437–442. [CrossRef]

32. Ion, M.; Berbecaru, C.; Iftimie, S.; Filipescu, M.; Dinescu, M.; Antohe, S. PLD deposited Al$_2$O$_3$ thin films for transparent electronics. *Dig. J. Nanomater. Biostruct.* **2012**, *7*, 1609–1614.

33. Ito, A.; Tu, R.; Goto, T. Amorphous-like nanocrystalline γ-Al$_2$O$_3$ films prepared by MOCVD. *Surf. Coat. Technol.* **2010**, *204*, 2170–2174. [CrossRef]

34. Ahn, C.H.; Kim, S.H.; Kim, Y.K.; Lee, H.S.; Cho, H.K. Effect of post-annealing temperatures on thin-film transistors with ZnO/Al$_2$O$_3$ su-perlattice channels. *Thin Solid Films* **2015**, *584*, 336–340. [CrossRef]

35. Tahir, D.; Kwon, H.L.; Shin, H.C.; Oh, S.K.; Kang, H.J.; Heo, S.; Chung, J.G.; Lee, J.C.; Tougaard, S. Electronic and optical properties of Al$_2$O$_3$/SiO$_2$ thin films grown on Si substrate. *J. Phys. D Appl. Phys.* **2010**, *43*, 255301. [CrossRef]

36. Greczynski, G.; Hultman, L. X-ray photoelectron spectroscopy: Towards reliable binding energy referencing. *Prog. Mater. Sci.* **2020**, *107*, 100591. [CrossRef]

37. Usman, M.; Arshad, M.; Suvanam, S.S.; Hallén, A. Influence of annealing environment on the ALD-Al$_2$O$_3$/4H-SiC interface studied through XPS. *J. Phys. D Appl. Phys.* **2018**, *51*, 105111. [CrossRef]

38. Guan, S.; Yamawaki, L.; Zhang, P.; Zhao, X. Charge-transfer effect of GZO film on photochemical water splitting of transparent ZnO@ GZO films by RF magnetron sputtering. *Top. Catal.* **2018**, *61*, 1585–1590. [CrossRef]

39. Qiao, Z.; Latz, R.; Mergel, D. Thickness dependence of In$_2$O$_3$:Sn film growth. *Thin Solid Films* **2004**, *466*, 250–258. [CrossRef]

40. Bouhdjer, A.; Attaf, A.; Saidi, H.; Benkhetta, Y.; Aida, M.; Bouhaf, I.; Rhil, A. Influence of annealing temperature on In$_2$O$_3$ properties grown by an ultrasonic spray CVD process. *Optik* **2016**, *127*, 6329–6333. [CrossRef]

41. Raj, A.M.E.; Lalithambika, K.; Vidhya, V.; Rajagopal, G.; Thayumanavan, A.; Jayachandran, M.; Sanjeeviraja, C. Growth mechanism and optoelectronic properties of nanocrystalline In$_2$O$_3$ films prepared by chemical spray pyrolysis of metal-organic precursor. *Phys. B Condens. Matter* **2008**, *403*, 544–554. [CrossRef]

42. Prabeesh, P.; Selvam, I.P.; Potty, S. Effect of annealing temperature on a single step processed Cu2ZnSnS4 thin film via solution method. *Thin Solid Films* **2016**, *606*, 94–98. [CrossRef]

43. Kavitha, V.; Suresh, S.; Chalana, S.; Pillai, V.M. Luminescent Ta doped WO$_3$ thin films as a probable candidate for excitonic solar cell applications. *Appl. Surf. Sci.* **2019**, *466*, 289–300. [CrossRef]

44. Deng, S.; Chen, R.; Li, G.; Xia, Z.; Zhang, M.; Zhou, W.; Wong, M.; Kwok, H.-S. High-performance staggered top-gate thin-film transistors with hybrid-phase microstructural ITO-stabilized ZnO channels. *Appl. Phys. Lett.* **2016**, *109*, 182105. [CrossRef]

45. Menéndez-Proupin, E.; Gutiérrez, G. Electronic properties of bulk γ−Al$_2$O$_3$. *Phys. Rev. B* **2005**, *72*, 035116. [CrossRef]

46. Costina, I.; Franchy, R. Band gap of amorphous and well-ordered Al$_2$O$_3$ on Ni3Al(100). *Appl. Phys. Lett.* **2001**, *78*, 4139–4141. [CrossRef]

47. Amirsalari, A.; Shayesteh, S.F. Effects of pH and calcination temperature on structural and optical properties of alumina nanoparticles. *Superlattices Microstruct.* **2015**, *82*, 507–524. [CrossRef]

48. Adamopoulos, G.; Thomas, S.; Bradley, D.D.C.; McLachlan, M.A.; Anthopoulos, T.D. Low-voltage ZnO thin-film transistors based on Y$_2$O$_3$ and Al$_2$O$_3$ high-k dielectrics deposited by spray pyrolysis in air. *Appl. Phys. Lett.* **2011**, *98*, 123503. [CrossRef]

49. Li, Z.; Ma, J.; Feng, X.; Du, X.; Wang, W.; Wang, M. Effect of thermal annealing on the optical and structural properties of γ-Al$_2$O$_3$ films prepared on MgO substrates by MOCVD. *Ceram. Int.* **2016**, *42*, 551–558. [CrossRef]

50. Dai, S.; Wang, T.; Li, R.; Wang, Q.; Ma, Y.; Tian, L.; Su, J.; Wang, Y.; Zhou, D.; Zhang, X.; et al. Preparation and electrical properties of N-doped ZnSnO thin film transistors. *J. Alloys Compd.* **2018**, *745*, 256–261. [CrossRef]